Composite Structures 134 (2015) 1014–1023

Contents lists available at ScienceDirect

Composite Structures

journal homepage: www.elsevier.com/locate/compstruct

Buckling of multiple discrete composite bundles in the elastomeric foundation of a curvature-morphing skin

A. Schmitz *, P. Horst

Institute of Aircraft Design and Lightweight Structures, TU Braunschweig, Hermann-Blenk-Straße 35, 38108 Braunschweig, Germany

ARTICLE INFO

Article history:
Available online 12 September 2015

Keywords:
Hybrid composites
Buckling
Elastic foundation
Morphing structures

ABSTRACT

A short introduction to curvature-morphing skins is given. The studied structure consists of outer hybrid layers (undergoing large curvature alterations in operation) with unidirectional discrete composite bundles embedded in an ethylene–propylene–diene rubber foundation. This work focusses on the crucial aspect of compressive behaviour along these bundles. In order to achieve a high performance, it is essential that the bundles do not reach their stability limit prior rupture due to exceeding the strength of the structure. Specimens are manufactured and tested in an appropriate set-up under almost real boundary conditions. A finite element unit-cell is implemented and validated. The boundary conditions and the manufacturing tolerances of the hybrid layer are investigated with respect to bundle-buckling. Finally, failure maps depending on key geometry parameters indicate a clear distinction between an out-of-plane and an in-plane buckling mode whereas the latter results in lower critical strains.

1. Introduction

This work focusses on the crucial aspect of span-wise strength within the development of a curvature-morphing skin for a gapless leading edge (droop nose) of an airliner's high-lift system designed by Burnazzi and Radespiel [1]. Although following investigations are motivated from the structural component point of view, the model-composite perspective allows to gain novel insights. In the following, a new experiment investigating the local buckling behaviour of compliantly embedded bundles is elaborately described. However, the demand of realistic boundary test conditions constitute an experimental challenge regarding the feasibility of local bundle-buckling while avoiding global sample instability.

1.1. Curvature-morphing skin

Structural adaption to operating conditions is an old but actual field of research in the aerospace sector. Especially continuous contour-variable airfoil (e.g. [2,3]) and wing (e.g. [4,5]) morphing offers increase of performance and possibilities [6]. Most morphing structures can be divided into an inner kinematic mechanism (acting as variable rib), an outer skin (smooth surface and taking local aerodynamic pressure) and an appropriate force transmission between both (solid enough but with minimum influence on the outer contour). However, this work is only on the behaviour of the skin. An overview of so far suggested skins is given by Thill et al. [7]. Regarding the structural characteristics, it can be distinguished between area-morphing (changing the wing area, usually at the trailing edge, e.g. [8,9]) and curvature-morphing (adaption of the wing profile, like a droop-nose [1]). It can be stated that recent morphing structures particularly benefit from high-performance fibre-reinforced composites, e.g. [10]. Obviously, morphing skins must simultaneously meet counteracting requirements, namely being highly deformable in morphing-direction while providing still enough stiffness and strength to counteract local aerodynamic pressure and loads originating from wing deflection. It turns out, that most structures try to meet these conflicting specifications by imposing an extreme anisotropy: a large compliance in morphing-direction is balanced by increased transverse stiffness.

However, in contrast to area-morphing, curvature-morphing skins most often need to feature a frequent change of their (bending) stiffness properties along the morphed contour. Therefore, the presented skin exhibits a layered structure (Fig. 1) and can thus be manufactured with standard composite tooling being a strong benefit compared to other candidates like e.g. corrugated composites [11,12]. In detail, the structural concept involves an inner fibre-reinforced plastics laminate extended with outer hybrid layers consisting of discrete composite bundles which are embedded in a compliant foundation. Presuming reasonable bond between all

* Corresponding author. Tel.: +49 (0)531 391 9910.
E-mail address: a.schmitz@tu-bs.de (A. Schmitz).

http://dx.doi.org/10.1016/j.compstruct.2015.09.004
0263-8223/

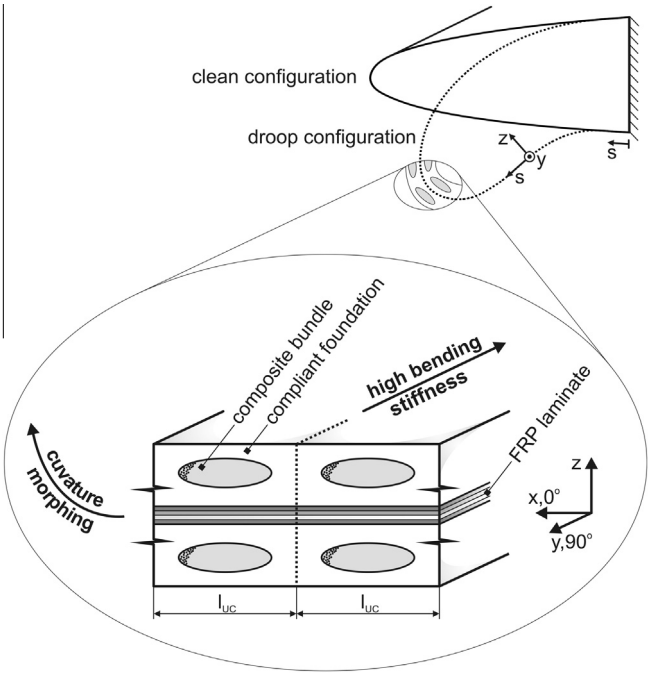

Fig. 1. Structural concept and application of the curvature-morphing skin. The replacement of the circumferential coordinate *s* by *x* at the unit-cell indicates a flat idealisation of a short curved skin segment.

structural parts, the foundation takes the high bending normal strains in morphing-direction, while the bundles generate large transverse (bending) stiffness. Note that the direct combination of technical fibres with a compliant matrix (known as chord-rubber composites, e.g. [13,14]) leads to very low bending and compressive strength due to a poor buckling support from the rubber-like matrix.

1.2. Motivation

The buckling behaviour along the discrete bundles oriented in span-wise direction is focussed on. From the structural point of view, the bundles ideally should provide a considerably higher critical buckling strain compared to the failure strain of the inner laminate, cp. Fig. 1. In this case, buckling failure must not be taken into account during sizing of an entire structure (e.g. droop nose). The second main aspect, namely the curvature at rupture in morphing-direction, is addressed in [15]. However, a most realistic experiment (in terms of operating boundary conditions) investigating the behaviour of bundle-buckling is set up. Additionally, a correspondent finite element unit-cell model with periodic boundary conditions is implemented and buckling is studied using linear eigenvalue instability analyses (only buckling initiation is of interest here). The outcome of the buckling test is intended to review the applicability of the numerical model and used theory. Precisely, the need of experimental data is motivated by the following aspects:

- The buckling problem is laying between the scales which are well described by existing theories. It is neither located at a micro-scale where one embedded fibre is completely surrounded by others, nor at a macro-scale with a single buckling column. In fact, it is an open question how an already buckled bundle influences the buckling performance of adjacent intact bundles. Hence, specimens always contain multiple bundles.
- Due to the unsymmetrical boundary conditions of the hybrid layers (foundation bonded to the inner laminate and opposite free surface), no stand-alone test of a hybrid layer using anti-buckling guides is possible as there is a considerable impact between bonded and unbonded contact of the foundation [16]. Additionally, it is unknown whether in-plane (xy-plane) or out-of-plane (yz-plane) buckling modes prevail.
- From studies of compressive failure mechanisms in standard composites (e.g. [17]) it is known, that apart from the fibre geometry, the shear strength and constitutive behaviour of the matrix as well as the fibre/matrix interface, initial fibre misalignment mainly affects the compressive performance. Particularly, the presented skin structure might suffer from an increased feasibility of bundle misalignment due to a co-curing manufacturing process (whole stacking is temporarily in a viscous phase) in combination with a large distance between individual bundles (compared to technical composites). In contrast, the numerical model assumes elastic buckling of initially straight bundles and linear elastic constitutive behaviour of the constituent materials. Thus, a certain expected overestimation (applies to most compressive failure models assuming ideal conditions) of the buckling performance must be quantified.
- The experimental scatter of compressive bundle failure is an open question. In order to separate impacts of different sources on the buckling performance, the scatter originating just from manufacturing tolerances within the xz-cross-section (excluding bundle misalignment) is evaluated by the numerical model.
- With an experimentally reviewed numerical model, the effect of adaptable geometric parameters on the buckling performance and behaviour can be estimated.

The paper is structured as follows. Section 2 details the constituent materials, the fabrication process and the specimen sizing. The determination of relevant geometric quantities needed as input for the modelling is described. The conducted buckling experiment is presented in Section 3. Afterwards, Section 4 deals with a correspondent finite element unit-cell model. Finally, Section 5 discusses the findings of this work and concludes the paper.

2. Specimens

This section specifies the constituent materials and presents considerations regarding the specimen sizing. Then, the fabrication process and the geometrical characterisation are detailed.

2.1. Materials

The inner laminate and the discrete bundles of the specimens are manufactured from unidirectional E-glass-fibres pre-impregnated with Hexcel's HexPly913® epoxy matrix (GFRP prepreg) with a nominal cured ply-thickness of 0.125 mm. The foundation is made of Kraiburg's AA6CFZ ethylene–propylene–diene rubber (EPDM) which is processed as 0.5 mm uncured sheet. Notably, this rubber compound is explicitly suitable to form a strong

Table 1
Material data of the constituent materials with subscripts $()_m$ for the epoxy matrix and $()_f$ for the glass-fibre properties of the HexPly913® prepreg.

GFRP HexPly913®			EPDM AA6CFZ		
E_m	3390	MPa	E	8.033	MPa
ν_m	0.380	–	ν	0.475	–
E_f	82,800	MPa			
ν_f	0.230	–			
V_f	55.5	%			

bond with epoxy resin during curing. The material data are given in Table 1. Here, the epoxy matrix properties E_m, ν_m and the cured fibre volume content V_f are taken from the manufacture's data sheet and with these the fibre properties E_f, ν_f are back-calculated from uniaxial tensile tests ($n = 5$) using the rule of mixture [18]. The EPDM properties originate from uniaxial tensile tests ($n = 4$), too. Without going into details, it can be stated that the EPDM starts to deviate from a linear constitutive behaviour at an uniaxial tensile strain of about 0.6%.

2.2. Sizing

The specimens deviate from a real curvature-morphing skin in terms of the thickness and stacking of the inner GFRP laminate. The chosen stacking is $[90_{HL}, 0, 90_{15}, 0, 90_{HL}]$ where 90_{HL} denotes a hybrid layer with a 90° (span-wise) bundle orientation, cp. Fig. 1. However, the thickness is a compromise. On the one hand the inner laminate is exposed to the same strain as the bundles. Thus, the ratio between bundle and inner laminate cross-section must be large enough to clearly detect buckling of a single bundle via the compressive force signal. On the other hand the specimens must be stiff enough to still withstand global Euler instability despite already failed bundles in order to continue the experiment. Note that the specimens become unsymmetrical throughout the experiment in case of unbalanced bundle buckling. This in turn causes a superimposed bending moment.

Although the specimens are well supported (Section 3), the compliant rubber surface admits a certain bending curvature (favouring Euler buckling and hence precocious global failure). In order to be able to capture this effect, each specimen is equipped with a HBM 1-LY13-3/120 strain gauge (SG), see Figs. 2 and 5, co-cured between one 0°/90° interface at the area of expected bundle buckling and oriented in compression-direction. Thereby, the SG solder contacts are led through the surface in order to be able to cut the samples later on. The 90° core is just to achieve large compressive strains (in a morphing application the inner laminate would rather be stacked primarily in 0°-direction). The incorporation of the 0° plies as border to the hybrid layers is motivated by the manufacturability. Namely, previous fabrication attempts taught that the bundle orientation must be different from the inner laminate border ply. Otherwise, the bundles dent the inner laminate during the manufacturing process (temporarily increased compaction pressure at the bundles due to local material accumulation).

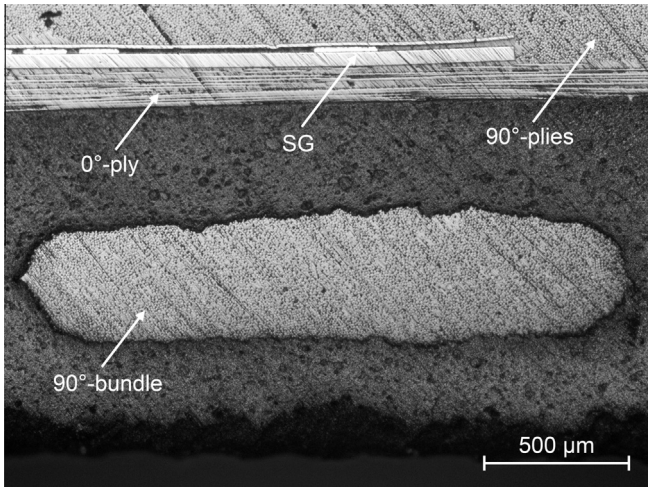

Fig. 2. Micrograph of a rubber embedded bundle (xz-plane, cp. Fig. 1). The inner GFRP laminate and the position of the co-cured strain-gauge (SG) are visible.

2.3. Manufacturing

Each hybrid layer is stacked from one macro ply of discrete bundles enclosed by two uncured rubber sheets. Before, the bundle ply is cut from a $[90_5]$ GFRP prepreg stack with a specially designed cutter head ensuring equal width and distances, see [15]. The interspace between individual bundles is not removed until the whole bundle ply has been draped. This technique allows to handle the bundles similarly to continuous prepreg stacks. Note, that the bundle cross section is initially rectangular after cutting and then cures to an ellipsoidal shape, see Fig. 2. The whole stacking is cured in a single autoclave process with 0.9 bar vacuum and 5 bar pressure at 125 °C. Finally, the specimens are cut from one plate (denoted HE5_90) with a diamond saw and grinded/polished to an extremely accurate rectangle oriented along the bundle-direction.

2.4. Geometry

The outer mean dimensions of the specimens are $L_y = 89.06$ mm) (compression-direction), $L_x = 19.27$ mm (always 6 bundles per width) and thickness $L_z = 4.63$ mm. In order to be able to setup models and compare them to the realised experiment, the exact geometry of the hybrid layers must be available, too. Thus, three polished specimens were taken at different positions of plate HE5_90 and five unit-cells of each polished section are measured with the microscope Zeiss Axio Lab.A1 (5x object lens). The geometrical parameters are denominated in Fig. 3. The correspondent mean values with Gaussian standard deviations are given in Table 2. Herein, unit-cells are divided between sides

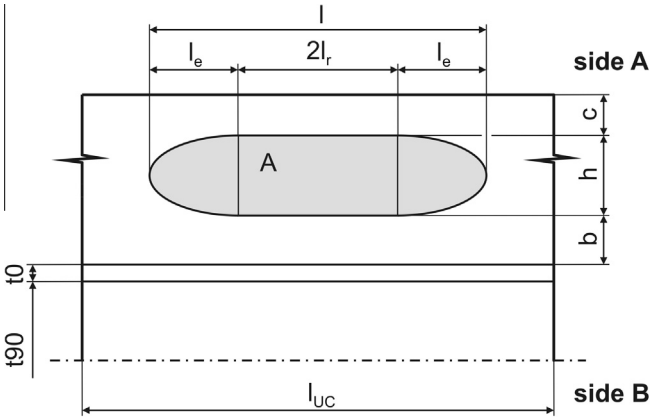

Fig. 3. Geometrical parameters of an unit-cell (UC).

Table 2
Geometry of plate HE5_90 split between either hybrid layers A and B. The inner laminate stack measures $t90 = 1863 \pm 25$ µm and the width of a repetitive unit-cell (cp. Figs. 1 and 3) $l_{UC} = 3200$ µm (given by cutter head adjustment and thus without standard deviation). Based on the measurement of 15 unit-cells.

HE5_90 side A				HE5_90 side B			
l_A	2081	±109	µm	l_B	2085	±98	µm
h_A	453	±22	µm	h_B	483	±24	µm
A_A	852510	±41569	µm²	A_B	893377	±31178	µm²
b_A	378	±22	µm	b_B	376	±15	µm
c_A	402	±24	µm	c_B	399	±22	µm
$t0_A$	121	±8	µm	$t0_B$	116	±8	µm

A and B as some geometrical parameters slightly differ from each other originating from the manufacturing process.

3. Experiment

The aim of the experimental investigation is to characterise the compressive failure of the compliantly embedded bundles. The following is split into an experimental set-up and a results section.

3.1. Set-up

The main demand on the experiment is the generation of most realistic test conditions with respect to the hybrid layers. However, in application both hybrid layers bond with their foundation to the inner GFRP laminate at one side and have a free surface on the other. Obviously, the inner laminate undergoes the same in-plane strain as the hybrid layers. Thus, as already mentioned in Section 1.2, the hybrid layers can neither be tested separately nor with continuous anti-buckling guides. Anyway, the specimens must be strongly supported against global instability because one objective of this experiment is to proceed until multiple bundles have been failed. At this point the influence of failed bundles onto their neighbours is captured. Additionally, it is also possible to measure a mean critical failure strain with correspondent scatter rather than a scatter of minimum values in case of terminating the test at first bundle failure. However, this means that a certain asymmetry (mainly the rising coupling term B_{22} in the sense of the classical laminated plate theory) should not cause early global failure.

For these reasons an appropriate fixture sketched in Fig. 4 is used. Herein, the specimen is prevented from global Euler buckling by supports inclined along the sample width and thus overlapping in compression-direction. In contrast, each single bundle features an unsupported length which equals the distance of the top and bottom support (as the bundle width is much smaller than the specimen). It is important to note, that the specimens are not clamped. Even if desired it would be impossible to transfer the load through the compliant rubber surface. In fact, the supports are individually adjusted to the exact thickness (in 0.05 mm steps) of each specimen by spacer discs, see Fig. 5. As consequence, the load is only transferred through the polished top and bottom faces. The resulting constant strain state throughout the whole length is advantageous. Namely, the compression strain can also be detected by an inductive displacement sensor (cp. Figs. 5 and 6). By comparing to the SG-strain, which is measured within the free-surface section, curvature deformations are detectable. Additionally, except the different surface support, boundary conditions are similar for the section between and inside the supports. Hence, despite the finiteness of the free-surface buckling length, the conditions meet reality as closely as possible. As the load is not transferred through the buckling supports there are no undesired induced shear strains by the inclination of the supports. The contact surface between specimen and support is equipped with a low friction Teflon film and the support inlets are provided with a 0.7 mm radius. The upper and lower supports are then placed between parallel guided ground steel plates which transfer the load to the specimens top and bottom surface. These plates are in turn mounted in an universal testing machine (Fig. 6) equipped with a 50 kN load-cell.

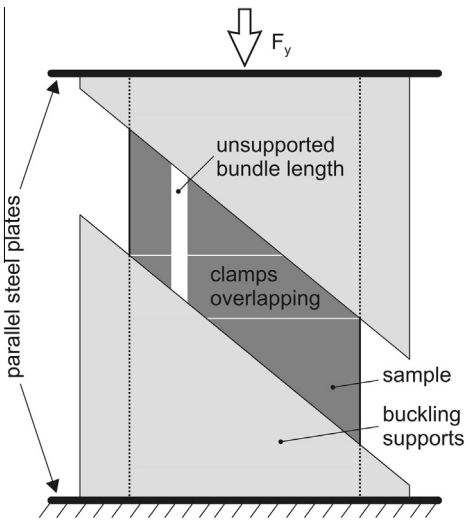

Fig. 4. Sketch and functionality of the fixture.

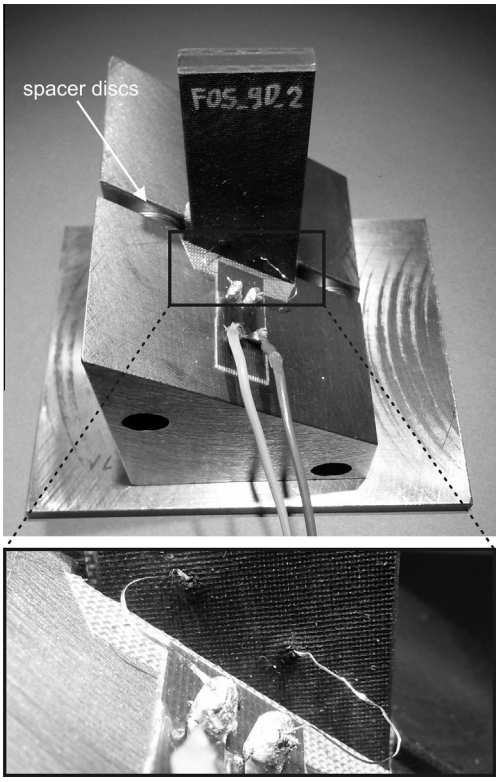

Fig. 5. Photograph of the fixture with one-sided mounted specimen. The thickness adjustment via spacer discs and a zoom of the strain gauge solder contacts are visible.

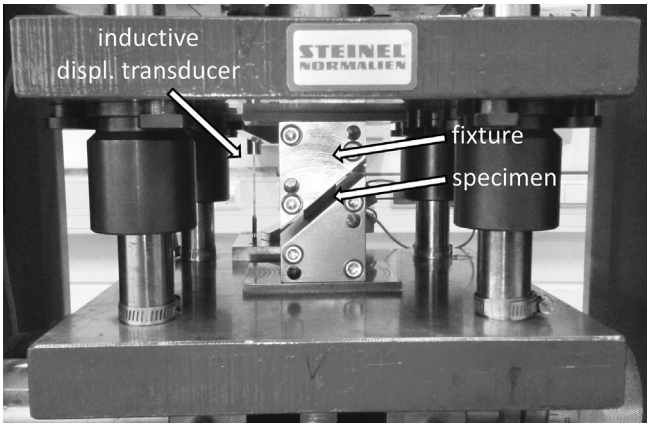

Fig. 6. Photograph of the experimental setup.

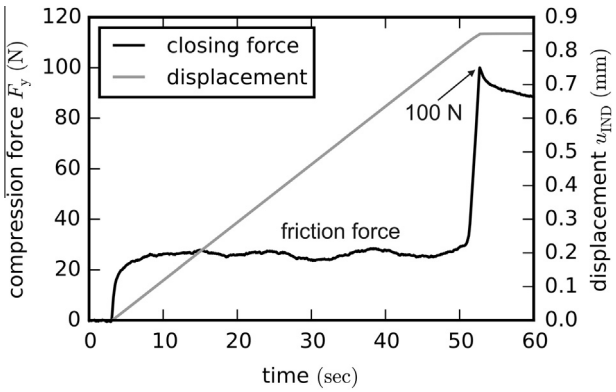

Fig. 7. Representative record of the closing procedure of specimen HE5_90_2 prior the actual test.

Before starting the main test, the supports are traversed together up to a compression pre-force of 100 N. Hereby, the upper support is fixed to the steel plate while the bottom support is self-aligning which avoids any destructive transverse constraining forces. After that, the length of the free-surface section measures 9.86 ± 0.04 mm $(n = 3)$. During closing, relatively constant forces generated by the wall friction between specimen and supports are recorded, see Fig. 7. The low friction forces of approximately 50 N (HE5_90_1), 26 N (HE5_90_2) and 20 N (HE5_90_3) illustrate the tight but not clamping adjustment.

After that, specimens are loaded with 1 mm/min and unloaded again directly after a clear drop (indicating global failure) of the compression force occurs. All data are sampled with 25 Hz in order to precisely detect bundle-buckling. It should be mentioned that there are constrained Poisson displacements in the specimen's thickness-direction. However, since the foundation is extremely compliant compared to the centred laminate, resulting through-thickness stresses and hence slightly increasing wall friction are negligible.

3.2. Results

A typical load/unload behaviour is plotted in Fig. 8. Herein, the compression force is displayed over the recorded strains obtained from the inductive displacement sensor (IND-strain) as well as the one-sided co-cured strain gauge (SG-strain). The following can be stated:

- Although the use of polished contact surfaces and a 100 N pre-force, there are still some settling effects differentiating both strain measurements.
- Final fracture is indicated by a distinct force drop (Fig. 8) always caused by breakage of a specimen's top or bottom face. This is due to a locally high surface pressure originating from exclusively loading the top and bottom faces in combination with a slightly unsymmetrical specimen behaviour.
- The IND-strain represents the in-plane normal strain and the SG-strain the normal strain with superimposed bending strain at the outside (side A) of the inner laminate. Both strains are valid until final failure. After that, only the SG-strain remains valid as the load transmission faces fail.
- Buckling of individual bundles can clearly be detected, see zoom in Fig. 8.

It is assumed that the SG-strain equals the bundle compression strain. This seems valid as there is only a very compliant connection between the bundles and the inner laminate via the foundation. Additionally, the top and bottom faces are not shear constrained as the specimens are not clamped within the supports. However, this assumption neglects the small thickness of the 0° border ply compared to the thick 90° core.

A comparison of the strain gauge bundle strain with the inductive in-plane strain is made for all specimens in Fig. 9. In order to circumvent the offset originating from the mentioned settling, only the first 0.8% IND-strains are plotted. Presuming a linear stress-flux/strain relation after settling, the slopes of the IND-strain curves are determined between 0.4% and 0.8% and extrapolated to the abscissa. The distances from this intersections to the origins of the SG-strains are then used as constant offsets to shift the whole IND-strain curves onto the SG-strain curves. This way, both strain measures can directly be compared.

Fig. 9 illustrates that IND and SG-strains almost equal each other as long as all bundles are intact. However, with an increasing number of buckled bundles, the slope of the SG-strain curves decrease compared to the IND-strains indicating a superimposed bending moment adding compressive strain to the SGs (located at sides A). The reason for this is that bundle buckling primarily

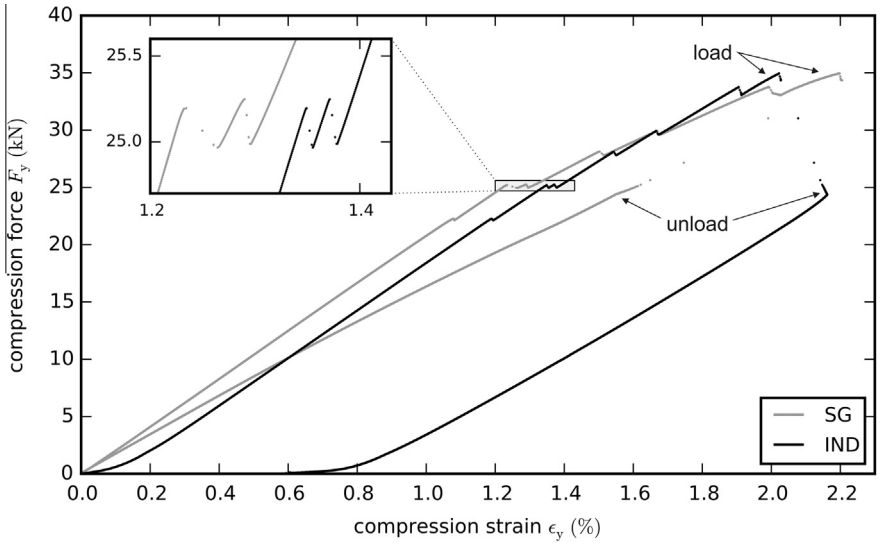

Fig. 8. Representative quasi-static load/unload cycle of specimen HE5_90_2. The compression force over strain gauge (SG) and inductive (IND) strain is displayed.

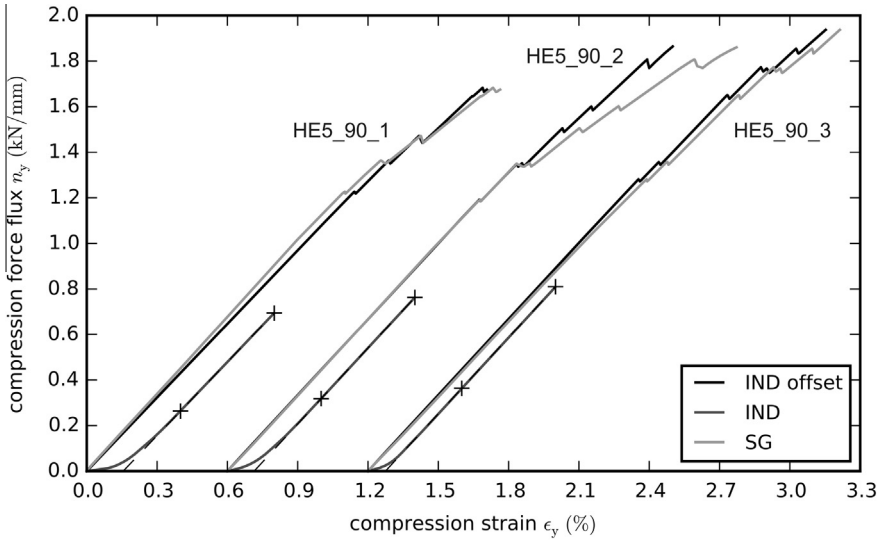

Fig. 9. Loading part of tested specimens displayed with an abscissa shift of 0.6% and 1.2% respectively. For each specimen the force flux over the strain-gauge (SG), inductive (IND) and offset inductive (IND offset) strain is plotted.

Table 3
Number of bundle buckling events per side A/B until final failure of the tested samples. There are always six bundles per side and width.

Specimen	Side A	Side B
HE5_90_1	4	1
HE5_90_2	6	1
HE5_90_3	6	0

occurred at sides A. A precise listing is given in Table 3. Originating from the manufacturing process, the mean cross-section of the bundles embedded at sides A is 4.8% smaller compared to these of sides B, see A_A and A_B in Table 2. As further investigated in Section 4.5 this results in slightly smaller critical buckling strains. Nevertheless, according to a statistical distribution, bundles can also buckle at sides B, which is most probable in case of an intact specimen (both sides suffer the same strain). With respect to Table 3 it can be stated that although this obviously happened twice, the average lower critical strains of sides A dominate. Finally, with rising asymmetry caused by one-sided bundle failure, buckling at the opposite hybrid layer becomes more and more unlikely.

Fig. 10 shows the free-surface area of a specimen after testing. Buckling failure is located centrally between both supports and follows their inclination. Obviously, bundle buckling leads to irreversible damage, see Fig. 11. From Figs. 10 and 11 it can be concluded that the critical buckling mode is an out-of-plane mode shape.

An overview of all specimens is presented in Fig. 12. Herein, the compressive force per sample width is plotted over the SG-strains and all buckling events are indicated. Based on 15 buckled bundles, the average experimental buckling strain with Gaussian standard deviation yields

$$\hat{\epsilon}_{exp} = 1.513 \pm 0.308\%. \quad (1)$$

However, buckling never occurs at exactly the same strain. Thus, any strong co-operative behaviour can be excluded. Indeed there are bundles buckling directly after each other. Hence, a certain buckling triggering imperfection induced by a buckled bundle onto the neighbours can not be excluded. In any case, the influence seems small.

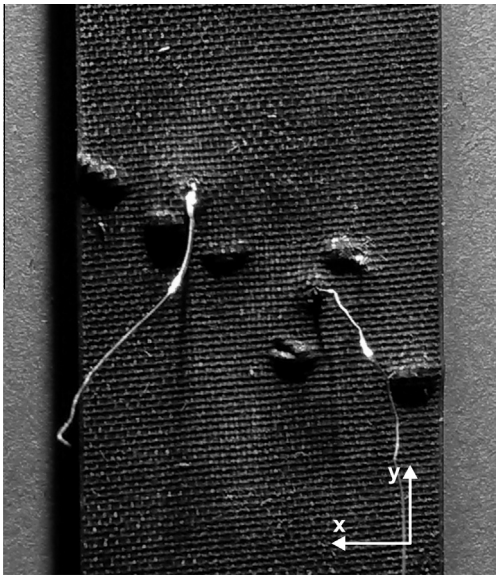

Fig. 10. Photograph of the region between the clamps of HE5_90_2 taken with sidelight (xy-view, cp. Fig. 1). All six bundles exhibit buckling damage.

4. Finite element analysis

The objective is to establish a proved buckling model. All analyses are conducted with the finite element package Abaqus/Standard®. First, a unit-cell model is set up. Afterwards, different configurations with accordingly varying buckling modes are introduced and results are compared with the experiment. Finally, failure maps varying key geometrical parameters are presented.

4.1. Theory

With the competing failure mechanisms of technical fibre reinforced plastics loaded in compression in mind [17], elastic and plastic micro-buckling come into consideration here. As there is no micro-buckling within the bundles but rather the whole bundles buckle, the constitutive behaviour of the rubber foundation is essential (distinction between both buckling types is mainly

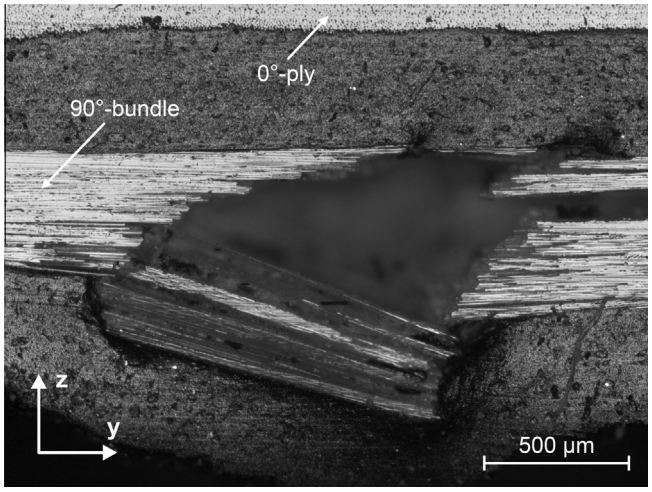

Fig. 11. Micrograph of a tested specimen at a buckling bump (yz-plane, cp. Fig. 1).

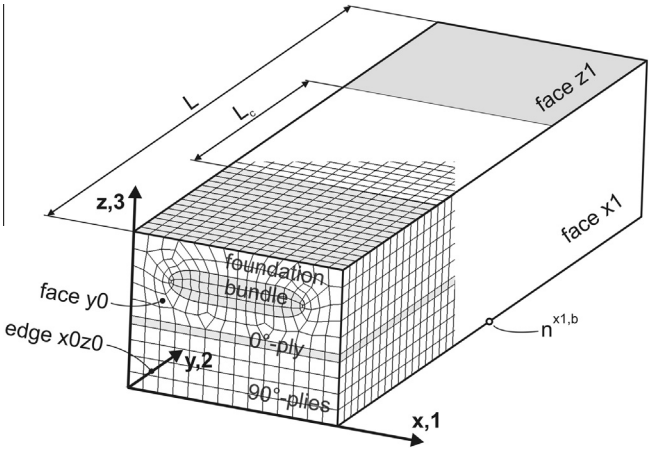

Fig. 13. Sketch of the finite element unit-cell with naming conventions and geometrical parameters. A typical mesh is illustrated in the front part.

determined by the constitutive behaviour of the matrix and initial local misalignment). As it is difficult to quantify initial misalignments and there was no plastification except the Mullins-effect during tensile tests of the foundation material, elastic buckling with perfectly oriented bundles is assumed. Additionally, it is expected that the critical buckling strain can reasonably be captured with a geometrical linear analysis. Note that the assumption of linear elastic buckling does not mean that this process is reversible. It is rather the trigger of rupture as the bundles fail by exceeding the material's strength.

4.2. Unit-cell model

Due to the symmetric stacking, a half-model is set up. Fig. 13 illustrates a typical finite element discretisation and defines the total length L and the free-surface length L_c of a repetitive bundle. The whole three-dimensional model is meshed with quadratic volume elements (C3D20R).

As the experiment shows no simultaneous buckling (and thus no distinct co-operative behaviour), it seems sufficient to analyse only one bundle per unit-cell here. Anyway, this has been reviewed by analyses of multiple bundles within one unit-cell. It turns out that the out-of-plane mode actually is periodical every two bundles ($n \times 2$). Herein, adjacent bundles are $\pi/4$ phase-shifted. However, the difference in terms of critical strain between one and two bundles per unit-cell is (depending on the exact bundle geometry but almost independent of the foundation stiffness) in the range of 3–4%. Additionally, Section 4.6 requires a model which is also valid for other buckling modes. Following [19], shear and transverse co-operative modes should be considered in case of possible in-plane buckling. Using periodic boundary conditions in x-direction, shear co-operative buckling can be analysed with a multiple of one bundle ($n \times 1$) whereas a transverse mode shape demands $n \times 2$ periodicity. However, regarding elastic microbuckling for technical composites, always the shear instability dominates [17]. Further, from [19], who built model composites with a comparably large modulus ratio of polyamide fibres to a silicon matrix, it can be deduced that an in-plane transverse co-operative buckling mode will not occur here. Nevertheless, some random sample configurations showing in-plane buckling of the failure maps in Section 4.6 are also calculated with two bundles to exclude this transverse mode. Further, it can be stated that the critical strain of a $n \times 1$ periodic shear mode differs by less than

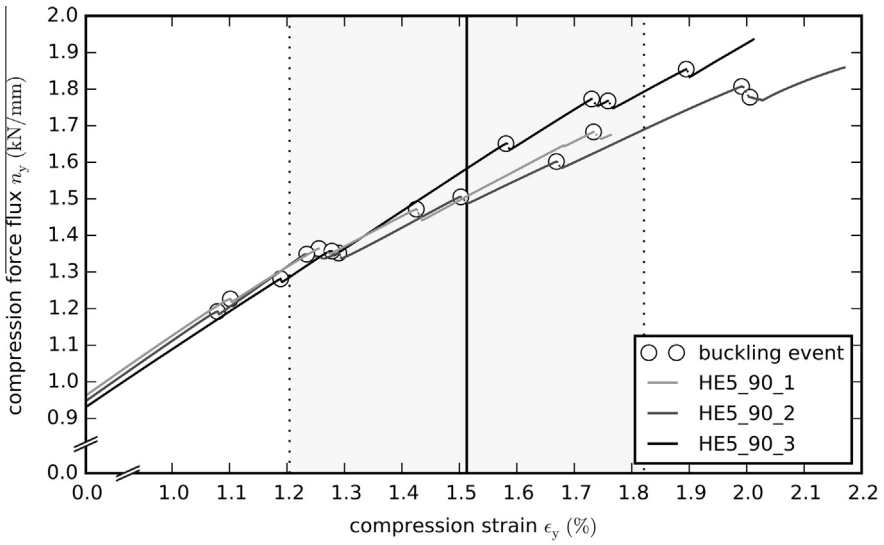

Fig. 12. Force flux over strain gauge strain (loading part) of all tested specimens. Bundle-buckling is indicated. The resulting mean buckling strain with Gaussian standard deviation is visualised.

0.5% between one and two bundles per unit-cell. Finally, due to calculation effort and experimental observations only a one bundle unit-cell is modelled.

Next, the bundle geometry is focussed on. A real bundle is visible in the micrograph of Fig. 2. However, the length l, height h and surface area A of the bundle can directly be measured (Table 2). The accordant idealisation of a rectangular middle section with length $2l_r$ and elliptical end-caps with semi-axis l_e is sketched in Fig. 3. The final shape is then obtained by the fragmentation of rectangle and ellipse by the measured bundle geometry via

$$l_r = \frac{4A - \pi lh}{2h(4-\pi)}, \tag{2}$$

$$l_e = \frac{4(lh - A)}{2h(4-\pi)}, \tag{3}$$

with $\pi/4 \cdot hl < A < hl$. Note, that l_e can either be the major or minor semi-axis.

4.3. Boundary conditions

The boundary conditions (BCs) are formulated based on the conventions given in Fig. 13 and [20]. In the following, all unstated degrees of freedom are always left unconstrained. First, there is the symmetry BC at face z0 setting all z-displacements to zero, hence $u_3^{z0} = 0$. The same holds for the (grey) part of face z1 located within the buckling supports, $u_3^{z1} = 0$. The compression strain is generated by applying a constant y-displacement at face y0 ($u_2^{y0} = \Delta u$) and fixing all y-displacements at the opposite face, $u_2^{y1} = 0$. The BCs at the x-faces must ensure periodic behaviour. As prerequisite all nodes at opposite faces must be located equally. Then, periodicity is implemented for all opposite node pairs i via explicit multiple point constraints (MPCs) by

$$u_\alpha^{x1,i} = u_\alpha^{x0,i} + \left(u_\alpha^{x1,b} - u_\alpha^{x0,b}\right). \tag{4}$$

Full periodicity in x-direction is assumed, thus $\alpha = 1, 2, 3$. The part in brackets of Eq. (4) enables global Poisson deformations. Precisely, periodic displacement fluctuations and also a varying (but constant throughout the model) width are possible. As the focus is set on the investigation of local bundle buckling, instability of the whole unit-cell must be excluded. Without restricting the afore mentioned BCs, full global stability is achieved by fixing the x-displacements of edge x0y0 ($u_1^{x0z0} = 0$) which suppresses buckling within the xy-plane. Potential global buckling within the yz-plane is inherently suppressed by the symmetry BC. These buckling BCs already suppress any rigid body translations and rotations.

4.4. Configurations

This section details the numerically investigated configurations. If nothing else is specified, the geometry of the unit-cell is according to the measured mean values of Table 2 (side A). Additionally, there is the configuration with BCs described in Section 4.3 (experiment configuration) and a second one according to application conditions (no-support configuration). The single difference of the no-support configuration is a complete zero-traction BC at face z1 (free surface).

With respect to calculation effort, configurations marked with a $()^\star$ indicate a shortened unit-cell length L, see Table 4. However, this should not considerably affect the results. Therefore, the influence of length L onto the two possible buckling modes (out-of-plane extension and in-plane shear mode) are investigated in Fig. 14. Hereby, two representative no-support configurations with different bundle length l are used. Note, that periodicity in bundle-direction can neither be exploited for the no-support configuration

Table 4
Definition of numerical boundary conditions and comparison with respect to the critical buckling strain. Herein, L denotes the total sample length and L_c the free surface section (cp. Fig. 13).

HE5_90 side A	L (mm)	L_c (mm)	$\hat{\epsilon}_A$ (%)
Experiment	89.06	9.86	1.773
Experiment*	40.00	9.86	1.774
No-support	89.06	89.06	1.664
No-support*	40.00	40.00	1.668

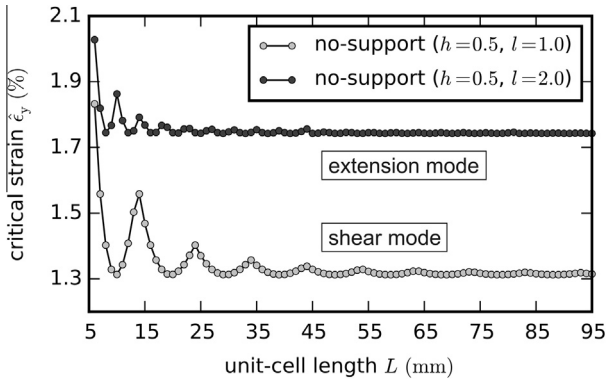

Fig. 14. Critical strain depending on the unit-cell length for two representative configurations showing the extension and shear eigenmode respectively.

as the afore unknown buckling wavelength must be available in advance. However, Fig. 14 illustrates that there is a minimum critical buckling strain every multiple of the buckling wavelength and that the maxima in between reduce with increasing unit-cell length. The slower convergence rate with respect to L in case of the shear mode is due to the longer wavelength, cp. Fig. 15. Thus, length $L = 40$ mm is chosen for the $()^\star$ configurations as compromise between accuracy and calculation time. A contour plot of both configurations showing the two possible modes is presented in Fig. 15.

The out-of-plane mode shapes of experiment* and no-support* are compared in the contour plot of Fig. 16. Obviously the topology of the critical buckling mode around the critical location of the experiment* configuration is similar to the critical no-support* mode. This also holds for the wavelength. Additionally, Table 4

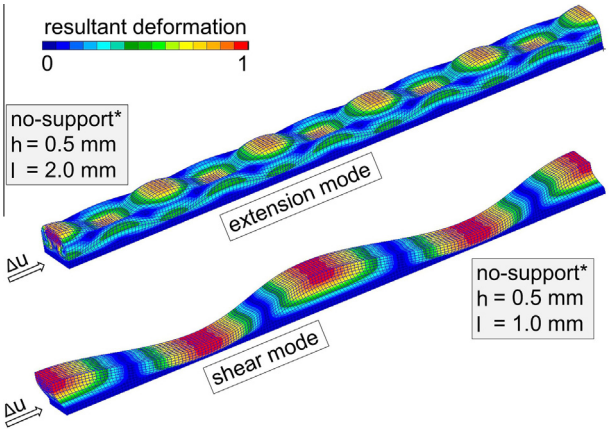

Fig. 15. Contour plot of the out-of-plane extension and in-plane shear eigenmode.

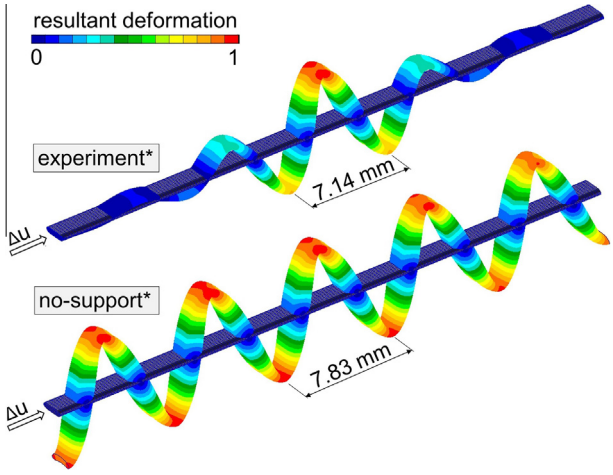

Fig. 16. Critical eigenmodes of the experiment (experiment*) and real application (no-support*) configuration. Buckling wavelength are given.

gives the critical buckling strains which differ only 6.1%. Hence, it is concluded that an experimental validation of the experiment* unit-cell can be assumed in case of the realistic no-support* model, too.

4.5. Validation

This section presents the analyses results of the corresponding experiment. All calculations use the experiment* configuration. The mean geometrical data in Table 2 are derived from 15 measured locations. Thereby, each location forms one geometry-set for side A and B respectively. As the geometrical parameters can not be assumed to influence the buckling behaviour linearly, all geometry-sets are individually analysed giving

$$\hat{\epsilon}_A = 1.779 \pm 0.094\%, \tag{5}$$

$$\hat{\epsilon}_B = 1.829 \pm 0.089\%. \tag{6}$$

All analyses show an out-of-plane extension mode which correlates with the experimental observation, repeat Fig. 10 and 11. The calculated lower critical buckling strain of side A due to the unit-cell cross section geometry (conditioned by the manufacturing process) matches with the observed distinct buckling at side A, cp. Table 3. Thus, the comparison of the numerical critical strain $\hat{\epsilon}_A$ (Eq. (5)) with the experimental $\hat{\epsilon}_{exp}$ (Eq. (1)) seems reasonable. It turns out that the mean measured buckling strain is about 15% lower than the calculated mean. The numerical Gaussian standard deviation is approximately 30% of the experimental one.

On the one hand, the expected lower value of $\hat{\epsilon}_{exp}$ is explained with geometrical imperfections along the bundles like initially slight local curvatures and misalignments. On the other hand there are induced imperfections. Although the experiment does not show clear co-operative buckling, a buckled bundle induces a certain stress field anyhow (remember the weak but existing $n \times 2$ periodicity of the out-of-plane mode). Obviously, this affects not immediately intact neighbours but of course might degrade the absolute critical strain. As the numerical deviation solely originates from the incorporation of geometrical fluctuations within the xz-plane, a large part of the residual 70% experimental standard deviation are associated with the above mentioned imperfections within the yz and xy-planes. Possible buckling favouring sources generated by a non-perfect experimental set-up are difficult to quantify.

4.6. Calculations

Having in mind that the presented numerical model with a one-bundle unit-cell and perfect geometry overestimates the performance of the real structure around 15%, buckling mainly influencing geometrical parameters of the bundle cross-section (Fig. 3) are investigated at this point. All calculations are performed with the no-support* configuration.

Generally, elastic micro-buckling is mostly influenced by the bending stiffness of the bundle and the effective foundation stiffness. Thus, in terms of cross-section geometry, these are the bundle height h, width l and foundation height b. Hereby, the bundle stiffness in x and y-direction trigger the transition between the out-of-plane and in-plane mode.

However, if b is varied all other parameters can be kept constant. In contrast, if l and h are changed, the bundle area A and the total unit-cell width l_{UC} must be adapted to preserve the geometrical unit-cell topology as expressed in Eqs. (2) and (3). For this reason, two geometrical constants are defined as

$$G_1 = l_{UC} - l, \tag{7}$$

$$G_2 = \frac{l_r}{l_e}. \tag{8}$$

With the mean values of the reference configuration (side A) these yield $G_1 = 1.119$ mm and $G_2 = 1.243$ respectively. Using these two definitions, it can be shown that with

$$A(l,h) = \frac{\frac{\pi}{4} + G_2}{1 + G_2} \cdot lh, \tag{9}$$

$$l_{UC}(l) = G_1 + l, \tag{10}$$

the ellipsoidal and rectangular fraction of the bundles (G_1) and also the difference between adjacent bundles (G_2) are kept constant.

With the above relationships Figs. 17 and 18 visualise the critical strain in dependence of b, l and h. Different modes are marked. The a priori measured mean unidirectional compression strain at rupture of the bundle composite in fibre-direction $\epsilon_{\parallel}^{-} = 2.58\%$ $(n = 5)$ is incorporated into the failure maps in case of being most critical. From Fig. 17 it is obvious that $\hat{\epsilon}_y$ exponentially rises in any cases with a higher foundation stiffness (smaller b). In contrast, a larger stiffness in bundle-direction (larger h) lets also increase $\hat{\epsilon}_y$ until a transition line from extension to shear mode. A similar downgrade is observed in Fig. 18. As long as the extension mode prevails, there is no dependence of l while $\hat{\epsilon}_y$ rises

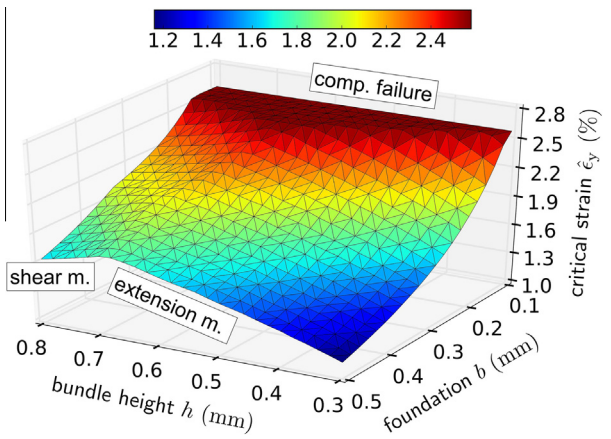

Fig. 17. Compressive failure in dependence of the foundation thickness b and bundle height h. The damage mechanisms shear and extension buckling as well as compressive strength failure are indicated.

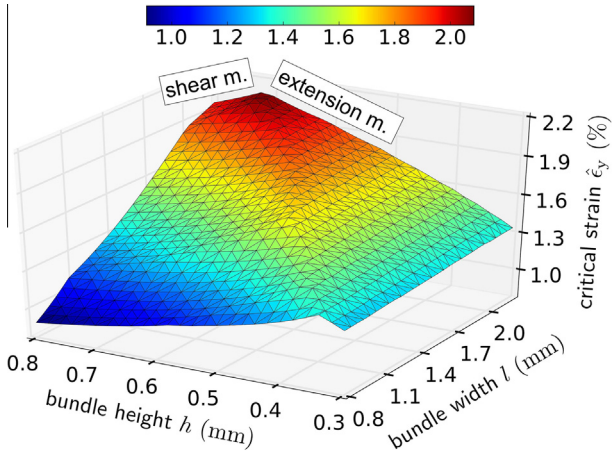

Fig. 18. Compressive failure in dependence of the bundle width *l* and height *h*.

with *h*. In contrast, the shear mode is mainly affected by the bending stiffness perpendicular to the bundle-direction. Thus, a larger *l* upgrades the buckling performance. It is important to realise that the positive larger *h* in case of extension is the opposite in case of a shear mode. Anyway, it can be extracted that the out-of-plane mode is advantageous. Note, that the slightly visible waviness within the shear mode area in both illustrations originates from the shortened unit-cell length in the no-support* configuration, cp. also Fig. 14.

5. Discussion and conclusion

A well described novel experiment investigating local buckling of compliantly embedded discrete composite bundles is presented. The difficulty of avoiding global instability of the tested specimen while enabling free local out-of-plane buckling is solved. Additionally, the quality of the experimental results benefits from the fact that bundle buckling mainly occurs at similar sides (sides A) of the nominal symmetrical specimens. Thus, similar geometries and strain measurement via the one-sided strain-gauge can be summarised for later comparisons. Nevertheless, a drawback of the presented fixture might be the short free (between the supports) specimen length. Namely, the large scaled bundle structure with respect to the essential free area (only one distinct critical location of the experimental buckling mode shape) might upgrade the experimental results due to a kind of size-effect. This means that the statistically available local cross-section (strongly influencing the total buckling performance) affects the results rather than the most critical location within the manufacturing tolerances along a bundle. Concluding, this further explains the large recorded standard deviation. Although only 3 specimens are tested, 18 of the volitional local buckling events are evaluated and compared to the finite element model.

The established finite element unit-cell overestimates the experimental buckling performance about 15% due to the made abstractions. Anyway, buckling failure maps investigating the influence of geometrical key cross-section parameters are generated with this model. However, as multiple cross-section geometries are measured, a next step would include the development of a non-linear calculated model with multiple bundles having different cross-sections. This would allow to investigate e.g. the impact of the foundation stiffness and geometry on the buckling coupling of adjacent bundles.

Acknowledgements

This work has been funded by the German Science Foundation (DFG) within the Collaborative Research Center 880 (SFB880).

References

[1] Burnazzi M, Radespiel R. Design and analysis of a droop nose for coanda flap applications. J Aircraft 2014;51(5):1567–79.
[2] Namgoong H, Crossley WA, Lyrintzis AS. Morphing airfoil design for minimum drag and actuation energy including aerodynamic work. J Aircraft 2012;49:981–90.
[3] Airoldi A, Crespi M, Quaranta G, Sala G. Design of a morphing airfoil with composite chiral structures. J Aircraft 2012;49:1008–19.
[4] Ghommem M, Hajj MR, Mook DT, Stanford BK, Beran PS, Snyder RD, et al. Global optimization of actively morphing flapping wings. J Fluid Struct 2012;33:210–28.
[5] Smith D, Ajaj R, Isikveren A, Friswell M. Multi-objective optimization for the multiphase design of active polymorphing wings. J Aircraft 2012;49:1153–60.
[6] Barbarino S, Bilgen O, Ajaj RM, Friswell MI, Inman DJ. A review of morphing aircraft. J Intell Mater Syst Struct 2011;22:823–77.
[7] Thill C, Etches J, Bond I, Potter K, Weaver P. Morphing skins. Aeronaut J 2008;112:117–39.
[8] Olympio KR, Gandhi F. Zero poissons ratio cellular honeycombs for flex skins undergoing one-dimensional morphing. J Intell Mater Syst Struct 2009:1–17.
[9] Olympio KR, Gandhi F. Flexible skins for morphing aircraft using cellular honeycomb cores. J Intell Mater Syst Struct 2010;21:1719–35.
[10] Kintscher M, Wiedemann M, Monner HP, Heintze O, Kühn T. Design of a smart leading edge device for low speed wind tunnel tests in the European project SADE. Int J Struct Integ 2011;2:383–405.
[11] Yokozeki T, Takeda S, Ogasawara T, Ishikawa T. Mechanical properties of corrugated composites for candidate materials of flexible wing structures. Compos Part A 2006;37:1578–86.
[12] Schmitz A, Horst P. Bending deformation limits of corrugated unidirectionally reinforced composites. Compos Struct 2014;107:103–11.
[13] Guynn EG, Ochoa OO, Bradley WL. Analysis of fiber microbuckling in thermoplastic composites. Int J Nonlinear Mech 1992;27:1039–47.
[14] Clark SK. Composite theory applied to elastomers. NASA contractor report 180322; 1986.
[15] Schmitz A, Horst P. A new curvature morphing skin: manufacturing, experimental and numerical investigations. In: Proceedings of the 16th European conference on composite materials, Seville, Spain; 2014.
[16] Papachristou KS, Sophianopoulos DS. Buckling of beams on elastic foundation considering discontinuous (unbonded) contact. Mechanics 2013;3:4–12.
[17] Fleck NA. Compressive failure of fiber composites. Adv Appl Mech 1997;33:43–117.
[18] VDI2014 A. Design and construction of fibre reinforced plastics components – basics. VDI; 1989.
[19] Müller C, Gorius A, Nazarenko S, Hiltner A, Bear E. Co-operative microbuckling of two fibres in a model composite. J Mater Sci 1996;31:2747–55.
[20] Schmitz A, Horst P. A finite element unit-cell method for homogenised mechanical properties of heterogeneous plates. Compos Part A 2014;61:23–32.